PAPER

Check for updates

Citric acid tuned negative thermal quenching of all inorganic copper-based perovskites†

Lu Yao, Hong Meng [ID] and Ming Liu*

Copper-based perovskites, with lower electronic dimensions and high photoluminescence quantum yields (PLQY), which are non-toxic and thermally stable, have been reported since 2019 and have immediately attracted great attention. So far, only a few studies have researched the temperature-dependent photoluminescence properties, posing a challenge in ensuring the stability of the material. In this paper, the temperature-dependent photoluminescence properties have been investigated in detail, and a negative thermal quenching of all-inorganic $CsCu_2I_3$ perovskites has been studied. Moreover, the negative thermal quenching property can be tuned with the assistance of citric acid, which has not been reported before. The Huang–Rhys factors are calculated to be 46.32/38.31, which is higher than for many semiconductors and perovskites.

1. Introduction

For luminescent materials, their photoluminescence (PL) intensity always decreases with an increase in temperature, which has been called thermal quenching.[1,2] However, a negative thermal quenching phenomenon has been found in some special luminescent materials, first discovered in doped GaAs and ZnS semiconductors.[3–6] This same phenomenon has then been found in pure ZnO material, GaInP, and carbon nanodots.[7–11] The reason for the negative thermal quenching is mostly attributed to electrons at defect energy states, which couple with phonons and can be easily activated by thermal energy.[3–11]

Perovskites, which were discovered in 1839, have received great attention in recent years due to the emergence of halide perovskites.[12–14] Significant developments have been made in light emitting, photodetector, and solar cell technologies concerning lead-halide perovskites.[15–19] However, these devices are severely affected by lead toxicity and poor thermal and air stability.[20–23] Copper-based perovskites, with lower electronic dimensions and high photoluminescence quantum yields (PLQY), which are non-toxic and thermally stable, were reported in 2019 and have received great attention immediately.[24–28] For instance, the all-inorganic $Cs_3Cu_2Br_{5-x}I_x$, which possess a 0D electronic structure, showed improved stability compared to that of Pb- and Sn-based halides.[29,30] $CsCu_2X_3$, which has a 1D electronic structure and multiple excitons, exhibits yellow light and has great potential for light emission.[25,31] Especially for

$CsCu_2I_3$, the single crystal of this material displays a high PLQY; the nanowire of it shows an intrinsic anisotropy due to its asymmetric structure and external morphology anisotropy, and exhibits polarization-sensitive photoconductive detection performance.[31–33] These materials are not only thermally stable in terms of their phase and structure, but also thermally stable in terms of their photoluminescence property.[32]

Chelating agents, such as polyvinylpyrrolidone, oleic acid, ethylene diamine tetraacetic acid, and citric acid, have been widely used to control particle size and crystal growth orientation in nanocrystal synthesis. In many reports, it has been shown that adding a chelating agent can significantly alter the crystallization and morphology of the nanocrystal, as well as its luminescence properties.[34–37] Herein, we report the negative thermal quenching phenomenon of the all-inorganic perovskite $CsCu_2I_3$, and we found that the negative thermal quenching property can be tuned by the chelating agent citric acid. In Roccanova *et al.*'s report, they also found a negative thermal quenching of $CsCu_2X_3$ structure, which they attributed to the "electron–phonon" coupling. However, in our experiment, we found the negative quenching not only attributed to electron–phonon coupling, but also highly related to the crystallinity and surface defects. To the best of our knowledge, this is the first report of chelating agents-tuned negative thermal quenching in perovskites, which provides a new strategy to enhance the luminescence and stability of perovskites.

2. Methods

2.1 Chemicals

All reagents were used without further purification, unless otherwise stated. Cesium iodide (CsI, Xi'an Polymer Light Technology Corp. 99.9%), copper iodide (CuI, Aladdin, 99.9%),

School of Advanced Materials, Peking University Shen Zhen Graduate School 2199 Lishui Road, Shenzhen 518055, P. R. China. E-mail: ddlm216@163.com

dimethyl sulfoxide (DMSO, Alfa Aesar, 99.9%), dimethyl formamide (DMF, S-A, 99.9%), citric acid (Cit, energy chemical, 99%), olic acid (OA, energy chemical, 99%) and methyl alcohol (Aladdin, 99%) are the original reagents.

2.2 Preparation

Synthesis of CsCu$_2$I$_3$ films. CuI (12.5×10^{-4} mol, 0.1187 g) and CsI (6.25×10^{-4} mol, 0.2436 g) with different amounts of Cit (0 mmol, 1 mmol, 2 mmol) were dissolved in 2.5 ml of a DMF : DMSO mixture (4 : 1, typically 2 ml DMF and 0.5 ml DMSO) and stirred at 60 °C in a nitrogen atmosphere until completely dissolved. The solutions were then filtered with a 0.22 μm nylon66 syringe and spin-coated onto quartz glass substrates. Each layer was deposited at 4000 rpm for 30 s and preheated at 100 °C for 1 h.

Synthesis of CsCu$_2$I$_3$ powders with Cit assistance. The residual precursor from the synthesis of CsCu$_2$I$_3$ films was then transferred to certain mount anti-solvent (methyl alcohol), forming a white powder in the process. The products were collected, separated by centrifugation, and dried at 60 °C in an atmosphere.

Synthesis of CsCu$_2$I$_3$ powders with OA assistance. CuI (12.5 $\times 10^{-4}$ mol, 0.1187 g) and CsI (6.25×10^{-4} mol, 0.2436 g) and different amounts of oleic acid (OA) (0 μl, 200 μl, 400 μl, 800 μl) were dissolved in 2.5 ml of a DMF : DMSO mixture (4 : 1, typically 2 ml DMF and 0.5 ml DMSO) and stirred at 60 °C in a nitrogen atmosphere until complete dissolution. The solution was then transferred to 2.5 ml of an anti-solvent (methyl alcohol), forming a white powder in the process. The products

were collected, separated by centrifugation, and dried at 60 °C in an atmosphere.

2.3 Characterization

The structural characterization of the CsCu$_2$I$_3$ films was carried out using an X-Ray Diffractometer (Bruker D8 Advance diffractometer with a Cu Kα (0.15418) X-ray source, operating at 80 KV and 40 mA). The measurements were taken from 2θ of 10° to 50°. The morphological characterization was conducted using a thermal field scanning electron microscope (ZeissSupra 55) operated at 5 kV and Atom force microscope (Bruker). Photoluminescence excitation and emission spectra were recorded with a photoluminescence spectrometer (HORIBA Fluorolog-3) equipped with a temperature control device. Absorption spectra were performed using a PerkinElmer lambda 950 spectrophotometer. Fourier transform infrared spectra were performed by a Fourier Transform Infrared Spectrometer (INVENIO-R).

3. Experiments and discussion

3.1 Structural and morphological studies

Structural characterization. To fully characterize the structure of the CsCu$_2$I$_3$ films, the X-ray diffraction (XRD) spectra of the three samples (Fig. 1(a)) were measured. For the samples with Cit amount of 0 mmol and 1 mmol, the phase are pure CsCu$_2$I$_3$ phase (PDF#45-0076) with a *CmCm* (63) space group. With further increasing the Cit amount to 2 mmol, the dynamic equilibrium of Cu$^+$ and Cs$^+$ in precursor might be changed,
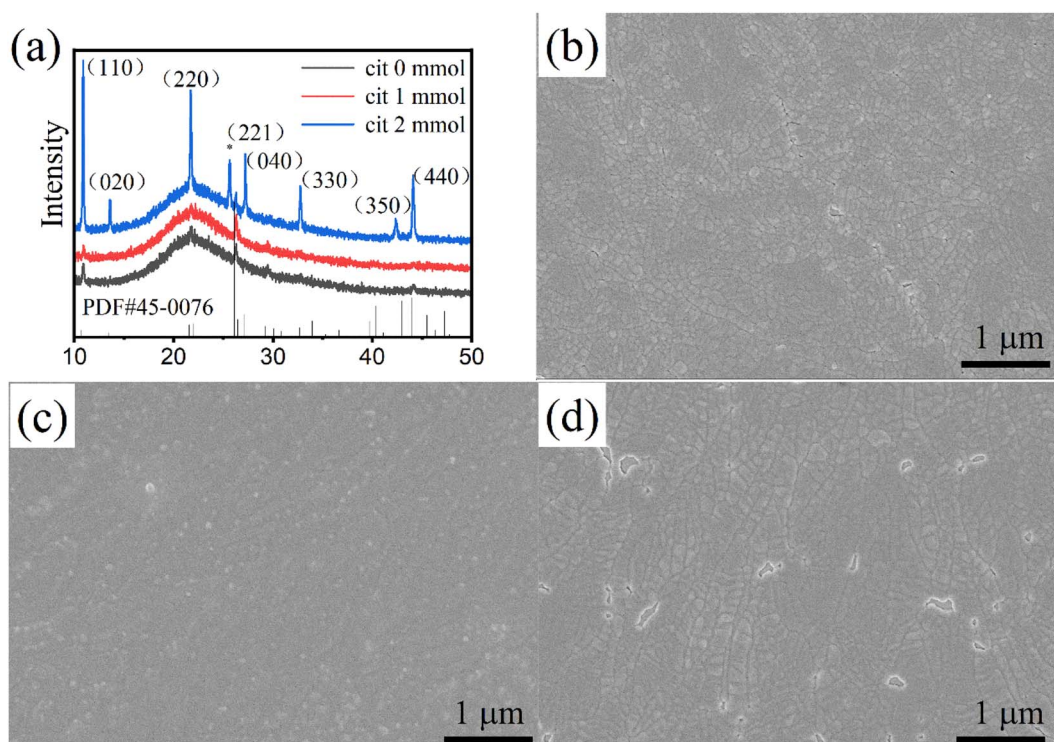

Fig. 1 (a) X-Ray diffraction patterns, and SEM images of the CsCu$_2$I$_3$ films with different Cit amounts (b) 0 mmol, (c) 1 mmol (d) 2 mmol.

a few impure phase $Cs_3Cu_2I_5$ (PDF#45-0077) with a *Pbnm* (62) space group can be observed, which are shown by a star symbol. As the amount of Cit increased, the XRD intensity become higher, implying a higher degree of crystallinity or a larger grain size. However, larger grain sizes can not be observed from the scanning electron microscopy (SEM) images (Fig. 1(b–d)). With Cit 0 mmol, a grain size of about 74 nm is obtained, and with Cit 1 mmol, it is hard to seen the grain boundary. The same results can also be obtained from AFM images (Fig S5†). Usually, Cit introduction leads to the orientation growth of crystals, but it is hard to identify the orientation growth from the films. Therefore, the micro-crystals have been synthesized by an anti-solvent method. The SEM images are shown in Fig. 2, and an obvious orientation growth can be observed with Cit added to the precursor. When there is no Cit in the precursor, the micro-crystals are 15 μm and there are lots of irregularly shaped powders. With Cit added to the precursor, the micro-crystals are 53 μm and the irregularly shaped powders has disappeared. From the analysis above, it can be concluded that the reason for the increasing XRD intensity might be due to better crystallinity and the orientation growth of the crystal.

3.2 Optical characterization

The absorption spectra of two samples with no Cit and 1 mmol Cit were measured and showed similar absorption performances, with a deep UV absorption less than 330 nm wavelength. The PL excitation spectrum (measuring emission at 550 nm) has two peaks at 314 nm (3.95 eV) and 323 nm (3.83 eV), with a peak spacing of 0.12 eV, which is close to the spin orbit splitting of copper d electrons. Previous reports have calculated the valence band (VB) and conduction band (CB) of $CsCu_2I_3$, with the results showing that the VB is mainly composed of Cu 3d orbitals and the CB derived from Cu 4 s orbitals. A VB splitting of 0.18 eV has also been reported before,[25] which is consistent with our results. The optical band gap (E_g) of $CsCu_2I_3$ thin films was calculated by the classical Tauc formula.[38]

$$\alpha h\nu = A(h\nu - E_g)^{1/2}$$

where A, h, ν, E_g, and α are constants, the Planck constant, light frequency, optical band gap, and absorption coefficient, respectively. The $(\alpha h\nu)^2$ *versus* $h\nu$ plots of $CsCu_2I_3$ films with different Cit amounts are shown in Fig. 3(b). The E_g can be obtained from the tangent line of the plots of Fig. 3(b). The E_g of $CsCu_2I_3$ films with no Cit and 1 mmol Cit are 3.7 eV, consistent with the previous reports of 3.93 eV, which have been calculated by hybrid PBE0 DFT calculations.[25,31] When the Cit amount increases to 2 mmol, the band gap is 3.43 eV, which shows a decrease due to the disturbance of the impure phase.

The PL spectra of $CsCu_2I_3$ films with different amounts of Cit were measured. All of the three samples shows a broad emission between 400 nm to 800 nm with an incident light of 325 nm.
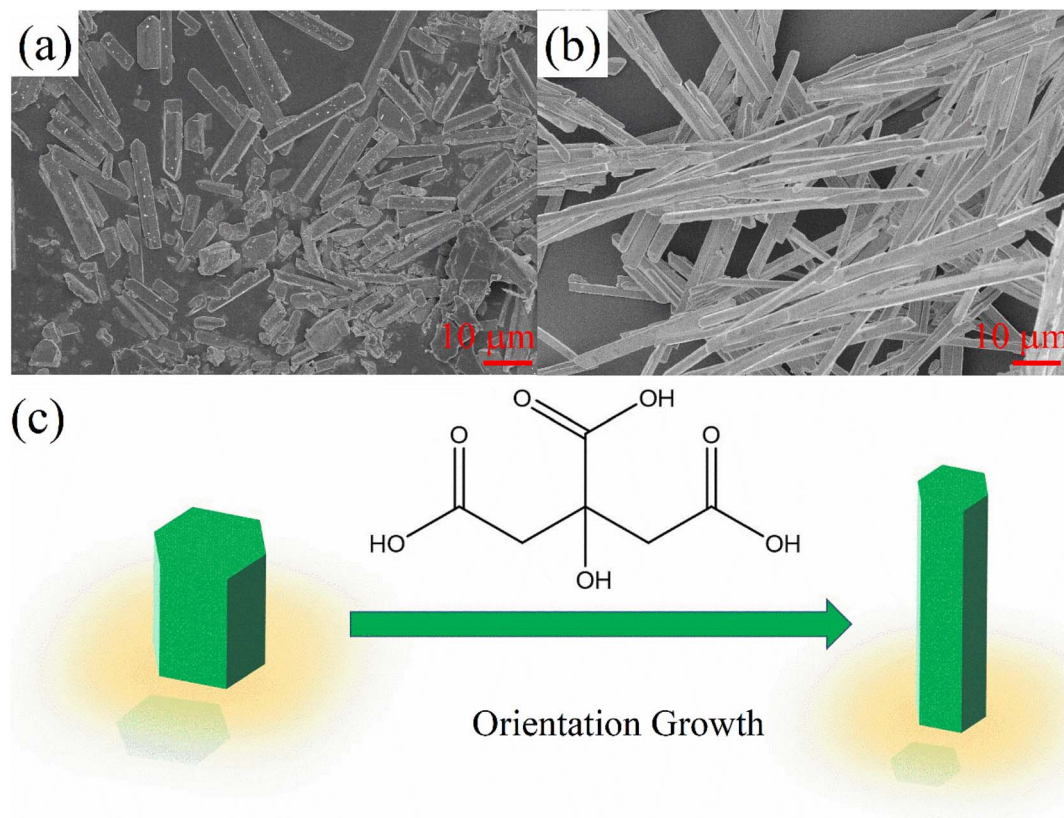

Fig. 2 SEM images of the $CsCu_2I_3$ micro-crystals with different Cit amounts (a) 0 mmol, (b) 1 mmol. (c) Schematic orientation growth of the $CsCu_2I_3$ micro-crystals with assistance of Cit.
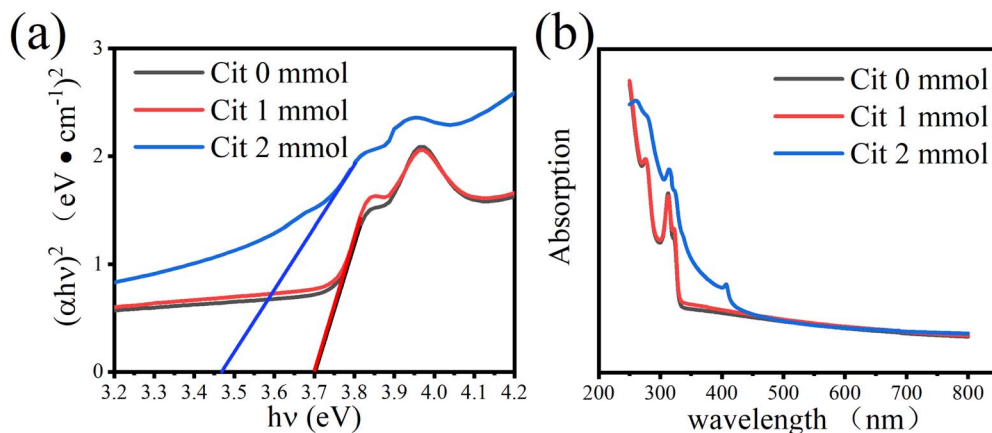
Fig. 3 (a) UV-visible absorption spectra (b) and the $(\alpha h\nu)^2$ *versus* $h\nu$ plots of $CsCu_2I_3$ films with different Cit amount.

The broad emission peak indicates that the electrons at the self-trapped states are coupling with the phonons.

The lifetime of the samples can be described by the equation:[39]

$$\tau = \frac{1}{\sum A_R + \sum A_{nR}}$$

$\sum A_R$ is the radiative transition rate of the samples, $\sum A_{nR}$ is the nonradiative transition rate of the samples. Fig. 4(b) shows the time-resolved PL of the as-prepared samples, from which the decay profile can be obtained by fitting with a two-exponential function. The sample with Cit 1 mmol shows the longest lifetime, which is 79 ns. The lifetimes of the samples with Cit 0 mmol and Cit 2 mmol are 67 ns and 60 ns, respectively. It is worth noting that with the addition of Cit to the precursor, the emission intensity has increased, indicating an increase in the radiative rate $\sum A_R$. However, the lifetime has increased, implying a decrease of narrative rate $\sum A_{nR}$. Therefore, we can conclude that the nonradiative rate has been efficiently suppressed due to the increasing crystallinity of the films, which has reduced localized disordered defects and limited the internal nonradiative pathway. However, with the Cit add into the precursor, there is as increase concentration of surface defects, which can be identified from the FTIR spectra (Fig. S7†). Even though the surface defects have increased, which would cause an increase of $\sum A_{nR}$, the combination of these two effects has ultimately caused a decrease of $\sum A_{nR}$ and an the increase of PL lifetime. With increasing Cit amount to 2 mmol, the lifetime shows a decrease, which may be attributed to the increased nonradiative rate of the impure phase $Cs_3Cu_2I_5$. The lifetime of the impure phase $Cs_3Cu_2I_5$ has also been measured, which is about 383 ns (Fig. S8†).

3.3 Temperature-dependents upconversion luminescence properties

The intensity of all $CsCu_2I_3$ samples first increases with temperature and then decreases at higher temperatures (Fig. 5(a and b)). For the $CsCu_2I_3$ sample with Cit 0 mmol, the highest PL integrated intensity is obtained at 200 K; for the $CsCu_2I_3$ sample with Cit 1 mmol, the highest PL integrated intensity is obtained at 250 K. From the structural and
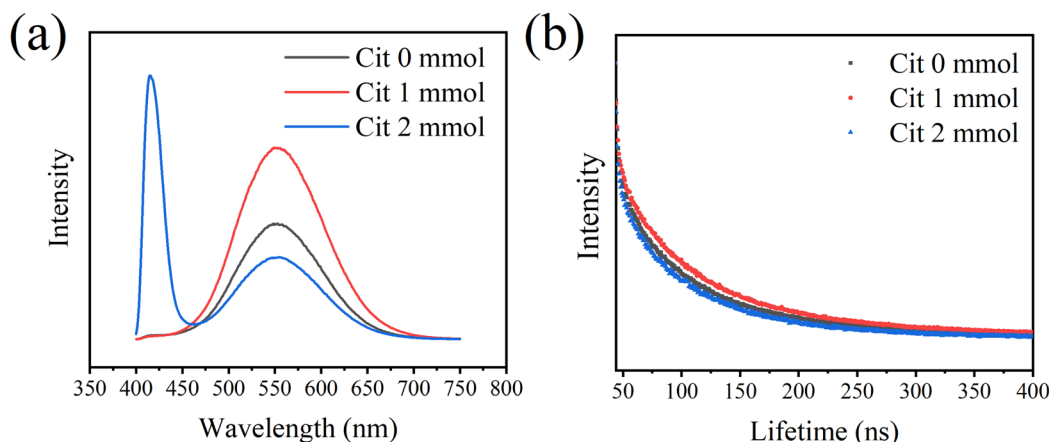

Fig. 4 (a) Photo luminescence (PL) spectra and (b) time resolved photo luminescence decay curves of $CsCu_2I_3$ films with different Cit amount (excited at 325 nm, emission at 550 nm).
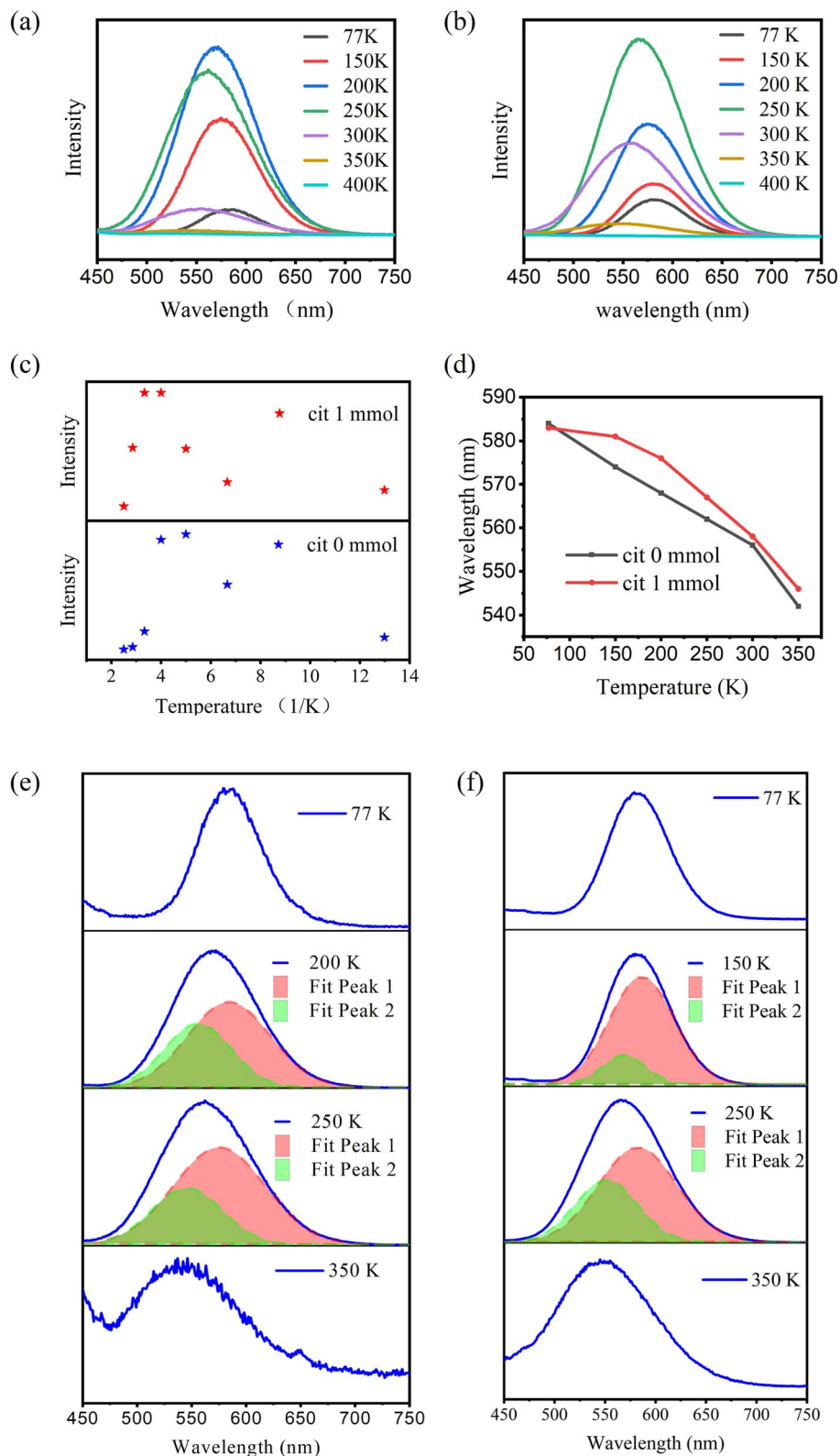
Fig. 5 (a and b) Temperature-dependent PL spectra of $CsCu_2I_3$ under 325 nm excitation. Thermal evolution of (c) integrated intensity, (d) peak position, (e and f) peak separation of PL peaks of $CsCu_2I_3$ with different Cit concentration.

morphology analysis, it can be observed that the samples with Cit 1 mmol have better crystallinity and more surface defects. Better crystallinity implies fewer defects in the crystal lattice.

Usually, the PL integrated intensity decreases with temperature, which is called "positive thermal quenching". In this experiment, the PL integrated intensity first increases with

temperature, and then quenches with temperature, which is called "negative thermal quenching". This phenomenon has been observed in some semiconductors and metal halides, which is attributed to the detrapping of electrons in defect states with increasing temperature.

The negative thermal quenching mechanism is illustrated by Fig. 6. The PL process can be described by the following path. First, the electrons at the valence band are activated to become hot-free electrons, and then the hot-free electrons turn into cooling-free electrons by carrier optical-phonon scattering. The cooling-free excitons then overcome the trap barrier by carrier acoustic phonon scattering and turn into self-trapped excitons. The self-trapped excitons couple with phonons by phonon scattering and phonon absorption, which form a broad emission band. Finally, the self-trapped excitons relax by non-radiative and radiative pathways. The nonradiative recombination is derived from the electrons at the defect energy state. The radiative recombination comes from the self-trapped excitons returning to the ground state directly. In the process, there are two different ways that account for the negative thermal quenching. First, the electrons at the surface defect energy state might be activated to the conduction band by increasing temperature. Second, the electrons at other defect energy states might be thermally activated to the self-trapped energy state.

The change in negative thermal quenching with different Cit amounts suggests that the negative thermal quenching of $CsCu_2I_3$ is mainly due to surface defects that have been thermally activated to the luminescence energy. To verify this conclusion, we synthesized micro-crystals by anti-solvent precipitation with the chelate agent OA. Due to the large size of the powder crystal, the surface-to-volume ratio becomes small, which will lead to low surface defect concentration, the temperature of the strongest luminescence intensity is lower than that of the $CsCu_2I_3$ films, which is around 150 K (Fig. S3†).

It also can be observed in Fig. 5(d–f) that there is a blue shift of the emission peak. It has been reported by Du's research that there is three self-trapped excitons in $CsCu_2I_3$ system. Two of them are at about 2.5–2.6 eV (blue emission). The other one at about 2.8 eV (green emission). Therefore, with the increasing temperature, there might be more electrons in defect energy detrapped to the self-trapped energy state with blue emission (Fig. 7).

The full width at half maximum (FWHM) are enlarged with increasing temperature, which implies electrons distributed to more self-trapped energy states as well, which is consistent with the blue shift results. In principle, the Huang–Rhys factor (S) reflects how strongly electrons couple to phonons, which can be obtained by fitting the temperature-dependent full-width at half-maxima (FWHM) of emission peaks using the equation as following;

$$FWHM = 2.36\sqrt{S}h\omega_{phonon}\sqrt{\coth\left(\frac{hw_{phonon}}{2k_B T}\right)}$$

where $h\omega_{phonon}$ is the phonon frequency. For $CsCu_2I_3$ with no Cit, S and $h\omega_{phonon}$ are calculated as 46.32 and 13.07 meV, respectively, For $CsCu_2I_3$ with Cit 1 mmol, S and $h\omega_{phonon}$ are calculated as 38.31 and 18.29 meV, respectively. The Huang–Rhys factor is larger than that of conventional emitters like CdSe, ZnSe and $CsPbBr_3$ perovskites, indicating the easy formation of STEs in $CsCu_2I_3$. However, the Huang–Rhys factor of $CsCu_2I_3$ are lower than many other perovskites, such as $Cs_3Sb_2I_9$, $Cs_3Bi_2I_9$ and $Rb_3Sb_2I_9$. It is comparable to a reported high quantum efficiency perovskite $Cs_2AgInCl_6$, of which the Huang–Rhys factor is 38.7, which means the photoluminescence performance of $CsCu_2I_3$ also can be good. But
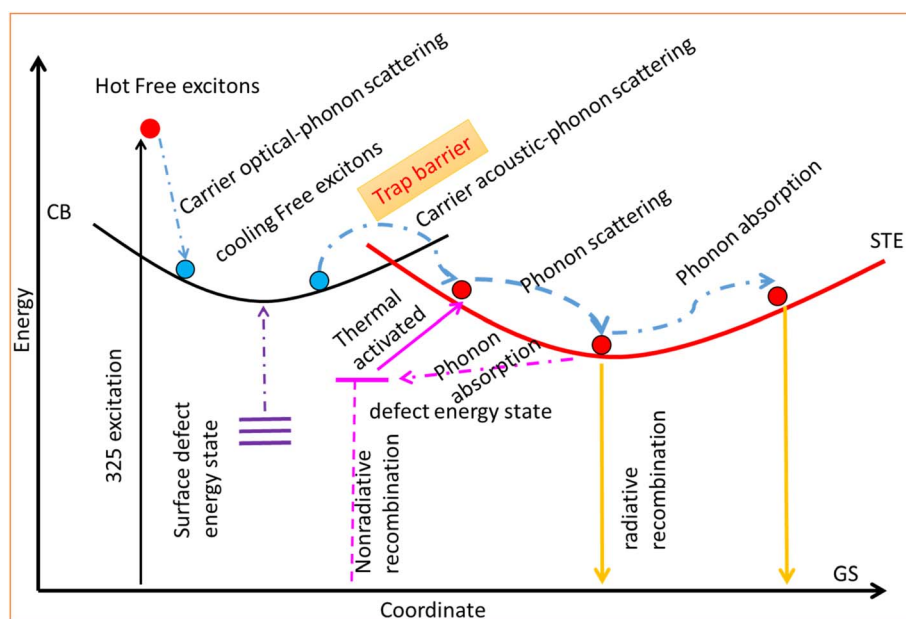

Fig. 6 Configurational coordinate diagram illustrating the origin of negative thermal quenching of as-prepared $CsCu_2I_3$ films.
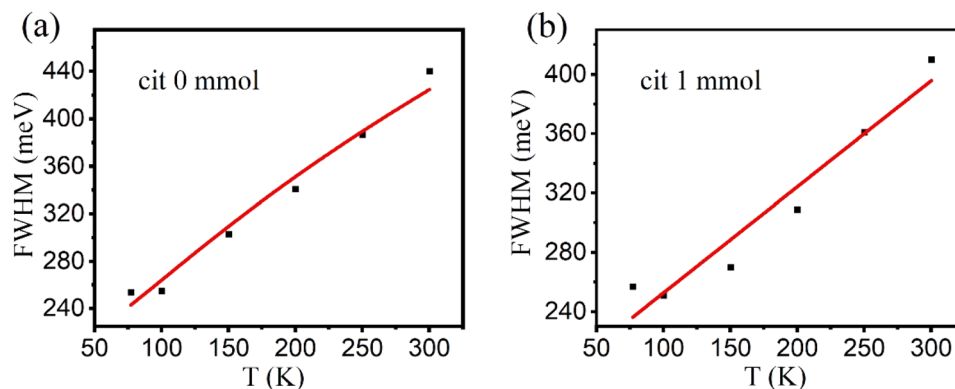
Fig. 7 (a and b) FWHM of $CsCu_2I_3$ with different Cit concentration.

Table 1 Huang–Rhys factors of different compounds

Compounds	Huang–Rhys factor	Ref.
CdSe	1	40
ZnSe	0.3	41
$CsPbBr_3$	3.2	42
$Cs_2AgInCl_6$	38.7	43
$CsCu_2I_3$	46.32/38.31	This work
$Cs_3Bi_2I_9$	79.5	44
$Rb_3Sb_2I_9$	50.4	44

unfortunately the emission peak (400–700 nm) is at the dual frequency peak of the excitation peak (328 nm), it hard to measure the QE of $CsCu_2I_3$ films (Table 1).

4.   Conclusion

Cit tuned negative thermal quenching photoluminescence performance has been found in the $CsCu_2I_3$, which has been derived from the increase of surface defect concentration. This enhanced negative thermal quenching performance improves the luminescence stability of $CsCu_2I_3$. This strategy provides a potential method to improve the luminescence stability of perovskites. The Huang–Rhys factor of $CsCu_2I_3$ films is higher than conventional emitters but lower than many perovskites, which is an appropriate value and implies that the $CsCu_2I_3$ films have good luminescence properties and potential applications in lighting and scintillator.

Conflicts of interest

There are no conflicts to declare.

Acknowledgements

References

1 F. E. Williams and H. Eyring, The Mechanism of the Luminescence of Solids, *J. Chem. Phys.*, 1947, **15**(5), 289–304.
2 H. Shibata, Negative Thermal Quenching Curves in Photoluminescence of Solids, *Jpn. J. Appl. Phys.*, 1998, **37**(Part 1, No. 2), 550–553.
3 R. Fivaz and E. Mooser, Electron–Phonon Interaction in Semiconducting Layer Structures, *Phys. Rev. [Sect.] A*, 1964, **136**(3A), A833–A836.
4 E. H. Bogardus and H. B. Bebb, Bound-Exciton, Free-Exciton, Band-Acceptor, Donor–Acceptor, and Auger Recombination in GaAs, *Phys. Rev.*, 1968, **176**(3), 993–1002.
5 D. Bimberg, M. Sondergeld and E. Grobe, Thermal Dissociation of Excitons Bounds to Neutral Acceptors in High-Purity GaAs, *Phys. Rev. B: Solid State*, 1971, **4**(10), 3451–3455.
6 J. Lee, E. S. Koteles and M. O. Vassell, Luminescence linewidths of excitons in GaAs quantum wells below 150 K, *Phys. Rev. B: Condens. Matter Mater. Phys.*, 1986, **33**(8), 5512–5516.
7 J. Gutowski, N. Presser and I. I. Broser, Acceptor-exciton complexes in ZnO: a comprehensive analysis of their electronic states by high-resolution magnetooptics and excitation spectroscopy, *Phys. Rev. B: Condens. Matter Mater. Phys.*, 1988, **38**(14), 9746–9758.
8 M. Watanabe, M. Sakai, H. Shibata, C. Satou, S. Satou, T. Shibayama, H. Tampo, A. Yamada, K. Matsubara, K. Sakurai, S. Ishizuka, S. Niki, K. Maeda and I. Niikura, Negative thermal quenching of photoluminescence in ZnO, *Phys. Rev. B: Condens. Matter Mater. Phys.*, 2006, **376–377**, 711–714.
9 W. K. Choi, H. C. Park, B. Angadi, Y. S. Jung and J. W. Choi, Negative thermal quenching in undoped ZnO and Ga-doped ZnO film grown on c-Al_2O_3 (0001) by plasma-assisted molecular beam epitaxy, *J. Electroceram.*, 2008, **23**(2–4), 331–334.
10 K. Wu, H. He, Y. Lu, J. Huang and Z. Ye, Negative thermal quenching of the 3.338 eV emission in ZnO nanorods, *Solid State Commun.*, 2012, **152**(18), 1757–1760.

© 2023 The Author(s). Published by the Royal Society of Chemistry

11 W. Junling, W. Rui, Y. Tiancheng, Z. Yong and W. Rong, Negative thermal quenching of the defects in GaInP top cell with temperature-dependent photoluminescence analysis, *Nucl. Instrum. Methods Phys. Res., Sect. B*, 2018, **414**, 1–3.

12 Y. Ling, L. Tan, X. Wang, Y. Zhou, Y. Xin, B. Ma, K. Hanson and H. Gao, Composite Perovskites of Cesium Lead Bromide for Optimized Photoluminescence, *J. Phys. Chem. Lett.*, 2017, **8**(14), 3266–3271.

13 M. Liu, G. Zhong, Y. Yin, J. Miao, K. Li, C. Wang, X. Xu, C. Shen and H. Meng, Aluminum-Doped Cesium Lead Bromide Perovskite Nanocrystals with Stable Blue Photoluminescence Used for Display Backlight, *Adv. Sci.*, 2017, **4**(11), 1700335.

14 V. V. Lemanov, A. V. Sotnikov, E. P. Smirnova, M. Weihnacht and R. Kunze, Perovskite CaTiO3 as an incipient ferroelectric, *Solid State Commun.*, 1999, **110**(11), 611–614.

15 L. Dou, Y. M. Yang, J. You, Z. Hong, W. H. Chang, G. Li and Y. Yang, Solution-processed hybrid perovskite photodetectors with high detectivity, *Nat. Commun.*, 2014, **5**, 5404.

16 M. A. Green, A. Ho-Baillie and H. J. Snaith, The emergence of perovskite solar cells, *Nat. Photonics*, 2014, **8**(7), 506–514.

17 H. Xu, R. Chen, Q. Sun, W. Lai, Q. Su, W. Huang and X. Liu, Recent progress in metal–organic complexes for optoelectronic applications, *Chem. Soc. Rev.*, 2014, **43**(10), 3259–3302.

18 H. Cho, S. H. Jeong, M. H. Park, Y. H. Kim, C. Wolf, C. L. Lee, J. H. Heo, A. Sadhanala, N. Myoung, S. Yoo, S. H. Im, R. H. Friend and T. W. Lee, Overcoming the electroluminescence efficiency limitations of perovskite light-emitting diodes, *Science*, 2015, **350**(6265), 1222–1225.

19 H. C. Yoon, H. Kang, S. Lee, J. H. Oh, H. Yang and Y. R. Do, Study of Perovskite QD Down-Converted LEDs and Six-Color White LEDs for Future Displays with Excellent Color Performance, *ACS Appl. Mater. Interfaces*, 2016, **8**(28), 18189–18200.

20 M. R. Filip, S. Hillman, A. A. Haghighirad, H. J. Snaith and F. Giustino, Band Gaps of the Lead-Free Halide Double Perovskites $Cs_2BiAgCl_6$ and $Cs_2BiAgBr_6$ from Theory and Experiment, *J. Phys. Chem. Lett.*, 2016, **7**(13), 2579–2585.

21 F. Giustino and H. J. Snaith, Toward Lead-Free Perovskite Solar Cells, *ACS Energy Lett.*, 2016, **1**(6), 1233–1240.

22 W. L. Hong, Y. C. Huang, C. Y. Chang, Z. C. Zhang, H. R. Tsai, N. Y. Chang and Y. C. Chao, Efficient Low-Temperature Solution-Processed Lead-Free Perovskite Infrared Light-Emitting Diodes, *Adv. Mater.*, 2016, **28**(36), 8029–8036.

23 T. C. Jellicoe, J. M. Richter, H. F. Glass, M. Tabachnyk, R. Brady, S. E. Dutton, A. Rao, R. H. Friend, D. Credgington, N. C. Greenham and M. L. Bohm, Synthesis and Optical Properties of Lead-Free Cesium Tin Halide Perovskite Nanocrystals, *J. Am. Chem. Soc.*, 2016, **138**(9), 2941–2944.

24 P. Vashishtha, G. V. Nutan, B. E. Griffith, Y. Fang, D. Giovanni, M. Jagadeeswararao, T. C. Sum, N. Mathews, S. G. Mhaisalkar, J. V. Hanna and T. White, Cesium Copper Iodide Tailored Nanoplates and Nanorods for Blue, Yellow, and White Emission, *Chem. Mater.*, 2019, **31**(21), 9003–9011.

25 M.-H. Du, Emission Trend of Multiple Self-Trapped Excitons in Luminescent 1D Copper Halides, *ACS Energy Lett.*, 2020, **5**(2), 464–469.

26 H. Chen, J. M. Pina, F. Yuan, A. Johnston, D. Ma, B. Chen, Z. Li, A. Dumont, X. Li, Y. Liu, S. Hoogland, Z. Zajacz, Z. Lu and E. H. Sargent, Multiple Self-Trapped Emissions in the Lead-Free Halide Cs3Cu2I5, *J. Phys. Chem. Lett.*, 2020, **11**(11), 4326–4330.

27 E. P. Booker, J. T. Griffiths, L. Eyre, C. Ducati, N. C. Greenham and N. J. L. K. Davis, Synthesis, Characterization, and Morphological Control of Cs_2CuCl_4 Nanocrystals, *J. Phys. Chem. C*, 2019, **123**(27), 16951–16956.

28 P. Cheng, L. Sun, L. Feng, S. Yang, Y. Yang, D. Zheng, Y. Zhao, Y. Sang, R. Zhang, D. Wei, W. Deng and K. Han, Colloidal Synthesis and Optical Properties of All-Inorganic Low-Dimensional Cesium Copper Halide Nanocrystals, *Angew. Chem., Int. Ed. Engl.*, 2019, **58**(45), 16087–16091.

29 Z. Luo, Q. Li, L. Zhang, X. Wu, L. Tan, C. Zou, Y. Liu and Z. Quan, 0D $Cs_3Cu_2X_5$ (X = I, Br, and Cl) Nanocrystals: Colloidal Syntheses and Optical Properties, *Small*, 2020, **16**(3), e1905226.

30 L. Xie, B. Chen, F. Zhang, Z. Zhao, X. Wang, L. Shi, Y. Liu, L. Huang, R. Liu, B. Zou and Y. Wang, Highly luminescent and stable lead-free cesium copper halide perovskite powders for UV-pumped phosphor-converted light-emitting diodes, *Photonics Res.*, 2020, **8**(6), 768–775.

31 R. Kentsch, M. Morgenroth, M. Scholz, K. Xu, J. Schmedt Auf der Gunne, T. Lenzer and K. Oum, Direct Observation of the Exciton Self-Trapping Process in $CsCu_2I_3$ Thin Films, *J. Phys. Chem. Lett.*, 2020, **11**(11), 4286–4291.

32 Z. Ma, Z. Shi, C. Qin, M. Cui, D. Yang, X. Wang, L. Wang, X. Ji, X. Chen, J. Sun, D. Wu, Y. Zhang, X. J. Li, L. Zhang and C. Shan, Stable Yellow Light-Emitting Devices Based on Ternary Copper Halides with Broadband Emissive Self-Trapped Excitons, *ACS Nano*, 2020, **14**(4), 4475–4486.

33 M. Zhang, J. Zhu, B. Yang, G. Niu, H. Wu, X. Zhao, L. Yin, T. Jin, X. Liang and J. Tang, Oriented-Structured CsCu₂I₃ Film by Close-Space Sublimation and Nanoscale Seed Screening for High-Resolution X-ray Imaging, *Nano Lett.*, 2021, **21**(3), 1392–1399.

34 S. Seth and A. Samanta, A Facile Methodology for Engineering the Morphology of $CsPbX_3$ Perovskite Nanocrystals under Ambient Condition, *Sci. Rep.*, 2016, **6**, 37693.

35 H. Lin, D. Xu, A. Li, D. Teng, S. Yang and Y. Zhang, Morphology evolution and pure red upconversion mechanism of beta-$NaLuF_4$ crystals, *Sci. Rep.*, 2016, **6**, 28051.

36 D. Gao, W. Gao, P. Shi and L. Li, pH- and surfactant-mediated tunable morphology and upconversion of rare-earth doped fluoride microcrystals, *RSC Adv.*, 2013, **3**(34), 14757–14765.

37 S. Ghosh, S. Paul and S. K. De, Control Synthesis of Air-Stable Morphology Tunable Pb-Free Cs_2SnI_6 Perovskite

Nanoparticles and Their Photodetection Properties, *Part. Part. Syst. Charact.*, 2018, **35**(9), 1800199.

38 R. Swanepoel, Determination of the thickness and optical constants of amorphous silicon, *J. Phys. E: Sci. Instrum.*, 1983, **16**(12), 1214–1222.

39 M. J. Weber, Probabilities for Radiative and Nonradiative Decay of Er^{3+} in LaF_3, *Phys. Rev. [Sect.] A*, 1967, **157**(2), 262–272.

40 V. Türck, S. Rodt, O. Stier, R. Heitz, R. Engelhardt, U. W. Pohl, D. Bimberg and R. Steingrüber, Effect of random field fluctuations on excitonic transitions of individual CdSe quantum dots, *Phys. Rev. B*, 2000, **61**(15), 9944–9947.

41 H. Zhao and H. Kalt, Energy-dependent Huang–Rhys factor of free excitons, *Phys. Rev. B*, 2003, **68**(12), 125309.

42 X. Lao, Z. Yang, Z. Su, Z. Wang, H. Ye, M. Wang, X. Yao and S. Xu, Luminescence and thermal behaviors of free and trapped excitons in cesium lead halide perovskite nanosheets, *Nanoscale*, 2018, **10**(21), 9949–9956.

43 J. Luo, X. Wang, S. Li, J. Liu, Y. Guo, G. Niu, L. Yao, Y. Fu, L. Gao, Q. Dong, C. Zhao, M. Leng, F. Ma, W. Liang, L. Wang, S. Jin, J. Han, L. Zhang, J. Etheridge, J. Wang, Y. Yan, E. H. Sargent and J. Tang, Efficient and stable emission of warm-white light from lead-free halide double perovskites, *Nature*, 2018, **563**(7732), 541–545.

44 K. M. McCall, C. C. Stoumpos, S. S. Kostina, M. G. Kanatzidis and B. W. Wessels, Strong Electron–Phonon Coupling and Self-Trapped Excitons in the Defect Halide Perovskites A3M2I9 (A = Cs, Rb; M = Bi, Sb), *Chem. Mater.*, 2017, **29**(9), 4129–4145.